Reduced endogenous Ca^{2+} buffering speeds active zone Ca^{2+} signaling

Igor Delvendahl[a,1], Lukasz Jablonski[a], Carolin Baade[a], Victor Matveev[b], Erwin Neher[c,1], and Stefan Hallermann[a,1]

[a]Carl-Ludwig-Institute for Physiology, Medical Faculty, University of Leipzig, 04103 Leipzig, Germany; [b]Department of Mathematical Sciences, New Jersey Institute of Technology, Newark, NJ 07102; and [c]Max-Planck-Institute for Biophysical Chemistry, 37077 Göttingen, Germany

Contributed by Erwin Neher, April 30, 2015 (sent for review March 9, 2015; reviewed by Gary Matthews and Bert Sakmann)

Fast synchronous neurotransmitter release at the presynaptic active zone is triggered by local Ca^{2+} signals, which are confined in their spatiotemporal extent by endogenous Ca^{2+} buffers. However, it remains elusive how rapid and reliable Ca^{2+} signaling can be sustained during repetitive release. Here, we established quantitative two-photon Ca^{2+} imaging in cerebellar mossy fiber boutons, which fire at exceptionally high rates. We show that endogenous fixed buffers have a surprisingly low Ca^{2+}-binding ratio (∼15) and low affinity, whereas mobile buffers have high affinity. Experimentally constrained modeling revealed that the low endogenous buffering promotes fast clearance of Ca^{2+} from the active zone during repetitive firing. Measuring Ca^{2+} signals at different distances from active zones with ultra-high-resolution confirmed our model predictions. Our results lead to the concept that reduced Ca^{2+} buffering enables fast active zone Ca^{2+} signaling, suggesting that the strength of endogenous Ca^{2+} buffering limits the rate of synchronous synaptic transmission.

active zone | calcium signaling | presynaptic | neurotransmitter release | calcium buffers

At presynaptic nerve terminals, the opening of voltage-gated Ca^{2+} channels during action potentials (APs) leads to a brief Ca^{2+} influx. The resulting microdomain Ca^{2+} signals reach several tens of micromolar amplitude near open Ca^{2+} channels and trigger neurotransmitter release at presynaptic active zones (1, 2). After Ca^{2+} channel closing, the binding to endogenous Ca^{2+} buffers and diffusion of Ca^{2+} within the cytosol lead to collapse of the microdomain, increasing the residual $[Ca^{2+}]$ in the presynaptic terminal to not more than a fraction of micromolar. During this equilibration with Ca^{2+} buffers, the majority of entering Ca^{2+} ions are bound to endogenous Ca^{2+} buffers (3). The strength of intracellular Ca^{2+} buffering can be characterized by the Ca^{2+}-binding ratio defined as the ratio of buffer-bound Ca^{2+} to free Ca^{2+} (4). It is established that strong Ca^{2+} buffering limits the spread of Ca^{2+} ions at active zones and thus restricts neurotransmitter release to the vicinity of Ca^{2+} channels (5). Rapid removal of calcium from the active zone is essential to sustain synchronous release during repetitive activity. However, the mechanisms controlling the speed of active zone Ca^{2+} signaling during repetitive synaptic transmission and the clearance of Ca^{2+} from the active zone in between APs remain elusive.

The cerebellar mossy fiber bouton (cMFB) to granule cell synapse is ideally suited to analyze Ca^{2+} signaling during repetitive synaptic transmission because of the synchronous neurotransmitter release at exceptionally high frequencies (6–8). Understanding rapid active zone Ca^{2+} signaling requires knowledge about the Ca^{2+} dynamics and the strength, mobility, and binding kinetics of endogenous Ca^{2+} buffers. In particular, a dissection of fixed and mobile buffers (9, 10) is needed, which is technically challenging and requires access to the presynaptic terminal.

Here, we perform quantitative two-photon Ca^{2+} imaging in cMFBs, which are dialyzed with the pipette solution, and in remote cMFBs along the same axon, which are minimally perturbed, to separately characterize fixed and mobile Ca^{2+} buffers. We show that rapid active zone Ca^{2+} signaling is achieved by a low Ca^{2+}-binding ratio of endogenous fixed buffers with low affinity and mobile buffers with high affinity. Our data explain how a central synapse achieves the speed of active zone Ca^{2+} signaling required for fast and synchronous transmitter release and suggest that the strength of endogenous Ca^{2+} buffering limits the precision and synchronicity of repetitive synaptic activity.

Results

Quantitative Two-Photon Ca^{2+} Imaging in cMFBs. Quantitative knowledge about presynaptic Ca^{2+} dynamics is crucial to understanding the mechanisms of active zone Ca^{2+} signaling. Here, we combined direct patch-clamp recordings from en passant cMFBs (6, 8) (Fig. 1 *A–C*) with quantitative two-photon Ca^{2+} imaging. Single APs produced distinct and reproducible fluorescence transients (Fig. 1 *D–F*), consistent with previous measurements in mice and turtles (11, 12). Presynaptic recordings permit quantifying Ca^{2+} transients using a dual-indicator method (13) (Fig. 1*G*). For each combination of Ca^{2+}-sensitive (green) and Ca^{2+}-insensitive (red) dye, the signals were calibrated with presynaptic recordings by adding 10 mM EGTA or 10 mM $CaCl_2$ to the intracellular solution (*Materials and Methods*). The Ca^{2+} concentration at rest ($[Ca^{2+}]_{rest}$) was 57 ± 7 nM in cMFBs based on recordings with the Ca^{2+} indicator OGB-1 (n = 30; Fig. S1*B*), consistent with other presynaptic terminals (14–16). Establishing quantitative two-photon Ca^{2+} imaging in combination with in-cell calibration measurements at cMFBs (Figs. S1 and S2) enabled us to analyze the Ca^{2+} dynamics at these presynaptic terminals in detail.

Significance

Calcium influx during action potentials triggers neurotransmitter release at presynaptic active zones. Calcium buffers limit the spread of calcium and restrict neurotransmitter release to the vicinity of calcium channels. To sustain synchronous release during repetitive activity, rapid removal of calcium from the active zone is essential, but the underlying mechanisms are unclear. Therefore, we focused on cerebellar mossy fiber synapses, which are among the fastest synapses in the mammalian brain and found very weak presynaptic calcium buffering. One might assume that strong calcium buffering has the potential to efficiently remove calcium from active zones. In contrast, our results show that weak calcium buffering speeds active zone calcium clearance. Thus, the strength of presynaptic buffering limits the rate of synaptic transmission.

Author contributions: I.D., E.N., and S.H. designed research; I.D., L.J., and C.B. performed research; V.M. and E.N. contributed new reagents/analytic tools; I.D., L.J., V.M., E.N., and S.H. analyzed data; and I.D. and S.H. wrote the paper.

Reviewers: G.M., SUNY Stony Brook; and B.S., Max Planck Institut für Neurobiologie.

The authors declare no conflict of interest.

Freely available online through the PNAS open access option.

[1]To whom correspondence may be addressed. Email: igor.delvendahl@medizin.uni-leipzig.de, eneher@gwdg.de, or hallermann@medizin.uni-leipzig.de.

This article contains supporting information online at www.pnas.org/lookup/suppl/doi:10.1073/pnas.1508419112/-/DCSupplemental.

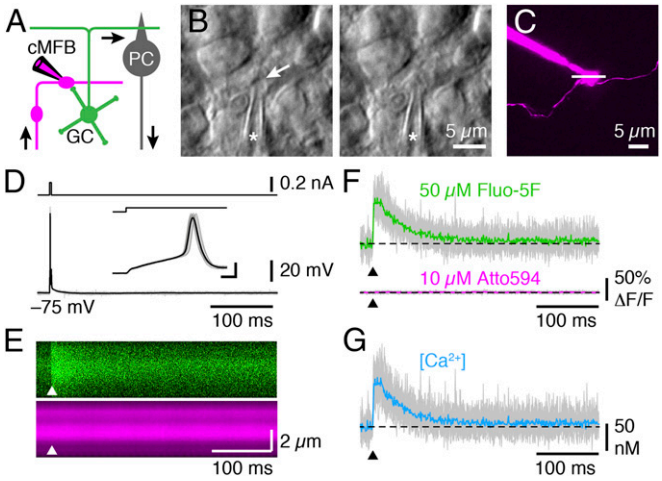

Fig. 1. Quantitative two-photon Ca^{2+} imaging in cMFBs. (*A*) Illustration of the cellular connectivity within cerebellar cortex. Mossy fibers (magenta) send information to the cerebellar cortex. Presynaptic cerebellar mossy fiber boutons (cMFBs) transmit signals to postsynaptic granule cells (GC, green), which excite Purkinje cells (PC, gray) via parallel fibers. Purkinje cell axons represent the sole output of the cerebellar cortex. Patch-clamp pipette illustrates presynaptic recording configuration. (*B*) (*Left*) Infrared image of a cMFB in an acute cerebellar slice during patch-clamp process. Arrow indicates membrane dimpling before seal formation. (*Right*) Same bouton after gaining whole-cell access. Asterisks indicate patch-pipette. (*C*) Two-photon image of a patched bouton filled with 10 μM Atto594 and 50 μM Fluo-5F (maximum z-projection of a stack of images over 45 μm; z-step, 2.5 μm). Line scan position is indicated. (*D*) cMFB APs elicited by current injection (200 pA, 3 ms). (*Inset*) APs on expanded time scale; superposition of 15 consecutive APs (gray) with average (black). (Scale bars, 200 μs and 20 mV.) (*E*) Two-photon line scans for the green and red channel. Arrowheads denote time point of AP. (*F*) Change in fluorescence intensity within the cMFB (ΔF/F) for the green and red channel. Colored traces are averages of 15 sweeps (gray). (*G*) Corresponding calculated Ca^{2+} concentration.

Low Ca^{2+}-Binding Ratio of Endogenous Fixed Buffers. The Ca^{2+}-binding ratio of endogenous fixed buffers ($\kappa_{E,fixed}$) can be estimated by loading a cellular compartment with various amounts of Ca^{2+} indicator dye (4, 17), as direct whole-cell recording from a small subcellular compartment leads to substantial wash-out of mobile Ca^{2+} buffers. We used Ca^{2+}-sensitive dyes of different affinities to measure Ca^{2+} transients evoked by single APs (Fig. 2 *A* and *B*). Increasing the Ca^{2+}-binding ratio of the added Ca^{2+} indicator (κ_B), which also acts as a Ca^{2+} buffer, reduced the amplitude and prolonged the decay of Ca^{2+} transients (Fig. 2 *A* and *B* and Fig. S3*A*). According to the single compartment model, the inverse of the amplitude (A^{-1}) and the decay time constant (τ) were linearly related to κ_B (4, 14) (Fig. 2 *C* and *D*). Hence, the Ca^{2+} transient without added buffer was estimated by linear extrapolation, yielding amplitude of 204 nM and τ of 50.3 ms. The Ca^{2+}-extrusion rate (γ) was determined as 267 s^{-1} and $\kappa_{E,fixed}$ as 17.1 and 12.5 from A^{-1} and τ extrapolation, respectively, resulting in a mean estimate of ∼15 (Fig. 2 *C* and *D*). The product of A and τ was independent of κ_B (18) (Fig. 2*E*). Statistical reliability was addressed with a bootstrap method, resulting in $\kappa_{E,fixed}$ of 17.5 ± 7.5 and 12.7 ± 7.2 from A^{-1} and τ extrapolation, respectively (mean ± SEM, corresponding to a 16–84% CI based on 152 experiments; *Materials and Methods* and Fig. S3*B*).

These results depend on correct quantification of presynaptic $[Ca^{2+}]$. To confirm that our two-photon imaging with dual-indicator calibration reliably estimates $[Ca^{2+}]$, we recorded Ca^{2+} transients in response to a single AP using the Ca^{2+} indicator Fura-2 and epifluorescence illumination with two alternating wavelengths (n = 12; Fig. 2*B*). The amplitude and decay time constant were in close agreement to the measurements with two-photon imaging (Fig. 2 *C* and *D*). Furthermore, a single-indicator method applicable for high-affinity Ca^{2+} dyes (being independent of intrabouton calibration measurements) (19) yielded very similar amplitudes (Fig. S3*A*). Thus, these data demonstrate that at cMFBs the Ca^{2+}-binding ratio of endogenous fixed buffers is very low compared with other presynaptic terminals (14, 15, 20–22).

Ca^{2+} Transients in Remote Boutons Indicate Wash-Out of Mobile Buffers. To analyze a potential wash-out of endogenous mobile buffers during presynaptic recordings, we measured Ca^{2+} transients in remote boutons along the mossy fiber axon of patched cMFBs (Fig. 3*A*). There, Ca^{2+} transients elicited by single APs became smaller in amplitude and decayed more slowly during dye loading (Fig. 3*B*). Intrabouton concentration and Ca^{2+}-binding ratio κ_B of Fluo-5F were calculated from the fluorescence intensity (Fig. 3 *C* and *D*). For quantification of Ca^{2+} signals, we corrected for a faster loading of Atto594 compared with Fluo-5F (*Materials and Methods*). Linear extrapolation of A^{-1} and τ vs. κ_B resulted in low and sometimes negative estimates of κ_E (Fig. 3 *E* and *F*). These results indicate a wash-out of slow mobile Ca^{2+} buffers, because slow buffers speed the decay of Ca^{2+} transients and the initial presence of slow buffers consequently leads to an underestimation of κ_E (23). Indeed, simulating the wash-in of

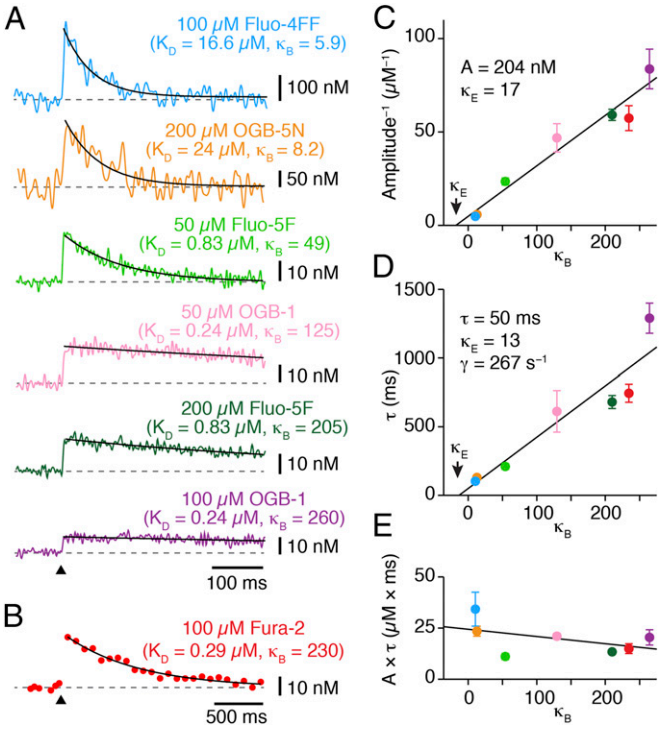

Fig. 2. Low Ca^{2+}-binding ratio of endogenous fixed buffers. (*A*) Example traces of Ca^{2+} transients in response to single APs recorded with different indicators (color-coded). Traces are averages of 25–30 sweeps and were digitally filtered for display (Fluo-4FF and OGB-5N examples were filtered to 100 Hz; remaining traces to 170 Hz). Black lines are exponential fits; arrowhead denotes time point of AP. The affinity (K_D) and Ca^{2+}-binding ratio (κ_B) of Ca^{2+} indicators are specified. (*B*) Example trace of Ca^{2+} transient in response to a single AP recorded with Fura-2 (average of 20 sweeps). (*C*) Inverse of the amplitude of AP-evoked Ca^{2+} transients recorded using different dyes plotted vs. Ca^{2+}-binding ratio of the indicator (κ_B). The line represents a linear fit. Extrapolation to the abscissa gave an estimate of the Ca^{2+}-binding ratio of endogenous fixed buffers (arrow). Color-coding is identical to *A* and *B*. (*D*) Corresponding analysis of the decay time constant (τ) of Ca^{2+} transients. Resulting parameters are indicated. (*E*) Product of *A* and τ plotted vs. κ_B. The line represents a linear fit.

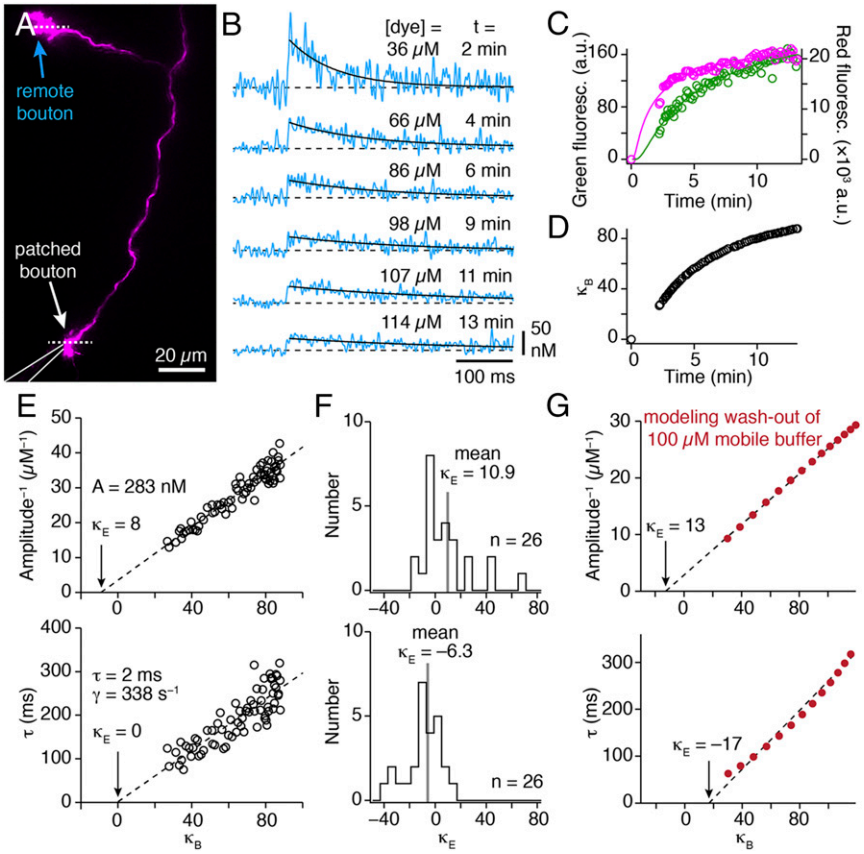

Fig. 3. Ca^{2+} transients in remote boutons indicate wash-out of a mobile buffer. (*A*) Two-photon image of a patched bouton filled with 10 μM Atto594 and 200 μM Fluo-5F (maximum z-projection of a stack of images over 80 μm; z-step, 4 μm; patch-pipette is illustrated schematically). Dotted lines indicate line scan positions in the patched and remote bouton. (*B*) Example traces of Ca^{2+} transients during dye loading in a remote bouton elicited by single APs at different time points after gaining whole-cell access. Time and estimated dye concentration are indicated; black lines represent exponential fits. (*C*) Red and green fluorescence at a remote bouton increase with time during whole-cell recording. Fluorescence was background subtracted and calculated over the whole trace (600 ms, red channel) or 90 ms of baseline before stimulation (green channel). Black lines are fits of Eq. **8**. (*D*) Ca^{2+}-binding ratio of added buffer (κ_B) vs. time. Dye concentration was calculated from the fit in *C*, and κ_B was computed using Eq. **5**. (*E*) Inverse of the amplitude (*Upper*) and time constant τ (*Lower*) of Ca^{2+} transients recorded during dye loading are plotted vs. κ_B. Lines represent linear fits; same experiment as in *B*. (*F*) Histograms of extrapolated κ_E values obtained from extrapolation of A^{-1} (*Upper*) and τ (*Lower*) in 26 dye loading experiments. Mean value is indicated in gray. (*G*) Simulating Ca^{2+} transients during dye loading and simultaneous washout of a slow endogenous buffer (100 μM mobile buffer with EGTA-like kinetics, red circles). Wash-out of the slow buffer impacts on τ-extrapolation, resulting in a negative κ_E estimate (dashed lines indicate linear extrapolation).

Fluo-5F and simultaneous wash-out of mobile buffers with slow binding kinetics reproduced well our observations (Fig. 3*G*).

To gain additional evidence that unperturbed cMFBs contain mobile Ca^{2+} buffers, we analyzed Ca^{2+} transients at the beginning of dye loading experiments. If a remote bouton was rapidly detected and recorded from, the initial concentration of added Ca^{2+} indicator was low ($\kappa_B < 15$; mean $\kappa_B = 9.0 \pm 1.3$; $n = 8$). Ca^{2+} transients at the beginning of these experiments decayed with a time constant of 51.2 ± 12.5 ms. Despite the presence of the Ca^{2+} indicator, the time constant is comparable to what the extrapolation to $\kappa_B = 0$ predicted for patched boutons ($\tau = 50$ ms; Fig. 2*D*). This observation again indicates that slow mobile buffers speed the decay of residual Ca^{2+} in cMFBs. We thus infer that cMFBs contain a substantial amount of endogenous mobile buffers.

Mobile Buffers at cMFBs Have Slow Bindings Kinetics. To gain insights into the properties of the mobile buffers, we compared Ca^{2+} transients in remote and patched boutons at identical dye concentration. In the dye loading experiments (Fluo-5F pipette concentration, 200 μM), we selected transients measured at ~50 μM Fluo-5F concentration (48.2 ± 2.1 μM, $n = 24$) during dye loading in remote cMFBs to compare with Ca^{2+} transients recorded using 50 μM Fluo-5F in separate experiments in patched cMFBs (Fig. 4*A*). The amplitudes were similar ($P = 0.75$), but the decay was significantly faster in remote compared with patched cMFBs ($P < 0.001$; Fig. 4*B*). This result is consistent with the presence of a mobile buffer with slow binding kinetics in remote boutons, because slow buffers speed the initial decay of the Ca^{2+} transient with little effect on amplitude (24). Note that the limited duration (500 ms) of our recordings precluded a detailed analysis of the slower exponential component resulting from the slow buffer, as discussed previously (25). However, including 100 μM EGTA in the patch-pipette reproduced the speeding of the initial decay time constant observed in remote boutons (Fig. 4 *A* and *B*). Furthermore, simulating the effect of mobile buffers with EGTA-like kinetics on the Ca^{2+} transient replicated well our results (Fig. S4 *A* and *B*). These data indicate that the endogenous mobile buffers at cMFBs have slow binding kinetics, high affinity, and are equivalent to ~100 μM EGTA (9).

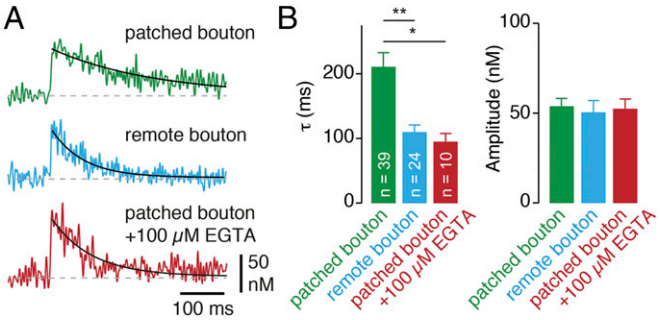

Fig. 4. Mobile buffers at cMFBs have slow bindings kinetics. (*A*) Example traces of Ca^{2+} transients evoked by a single AP. (*Top*) Ca^{2+} transient at a patched bouton recorded with 50 μM Fluo-5F. (*Middle*) Ca^{2+} transient recorded with 46 μM Fluo-5F in a remote bouton at the beginning of dye loading (200 μM Fluo-5F in the pipette solution). (*Bottom*) Ca^{2+} transient at a patched bouton measured with 50 μM Fluo-5F and 100 μM of the slow Ca^{2+} buffer EGTA. Traces are single sweeps. (*B*) Decay time constant (τ) and amplitude of Ca^{2+} transients evoked at patched (green) or remote boutons (blue) and with EGTA added to the pipette solution (red). The estimated concentration of Fluo-5F at remote boutons in the initial phase of dye loading was 48.2 ± 2.1 μM ($n = 24$), which is comparable to the Fluo-5F concentration in patched cMFBs (50 μM).

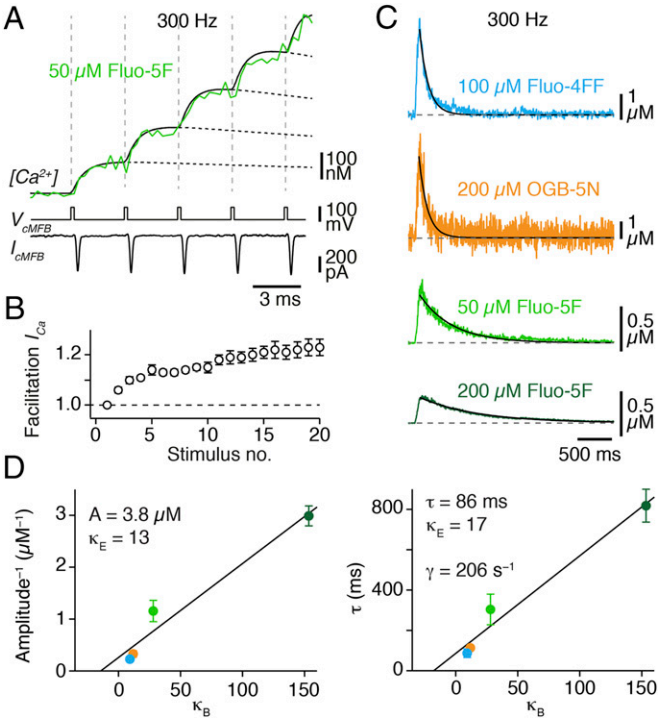

Fig. 5. Buildup of residual Ca^{2+} concentration during high-frequency firing. (*A*) (*Top*) Ca^{2+} concentration measured during the first five stimuli of 300-Hz AP firing in a cMFB with 50 μM Fluo-5F (3-kHz temporal resolution) superimposed with the prediction of our model. (*Middle*) Voltage command. (*Bottom*) Corresponding presynaptic Ca^{2+} currents. Note the facilitation of the peak Ca^{2+} current amplitude. (*B*) Average peak Ca^{2+} currents amplitude during high-frequency trains normalized to the first amplitude and plotted vs. stimulus number ($n = 5$ cells). (*C*) Example traces of Ca^{2+} transients in response to a train of 20 APs at a frequency of 300 Hz measured with different Ca^{2+} indicators. Traces are averages of two to five sweeps; black lines represent exponential fits. (*D*) Inverse of the amplitude and time constants (τ) of Ca^{2+} transients in response to 20 APs at 300 Hz vs. κ_B. Lines represent linear fits; color-coding is identical to *C*.

Buildup of Residual Ca^{2+} During High-Frequency Firing. In vivo, cMFBs fire bursts of APs with exceptionally high frequencies (6, 26), where vesicular transmitter release is remarkably synchronous (8, 27). To understand which mechanisms enable synchronous high-frequency release, we measured the buildup of Ca^{2+} during high-frequency bursts (20 APs at 300 Hz). First, we analyzed the Ca^{2+} influx per AP during train stimulation by pharmacologically isolating the Ca^{2+} current elicited by AP-like stimuli (200 μs to 0 mV; Fig. 5*A*). Ca^{2+} currents displayed facilitation during 300-Hz bursts (Fig. 5*B*), consistent with P/Q-type voltage-gated Ca^{2+} channels at cMFBs (8). Next, we used Ca^{2+} imaging to measure the increased spatially averaged residual [Ca^{2+}] by 300-Hz train stimulations (Fig. 5*C*). The increase caused by individual APs could be resolved well and appeared constant for the first APs of the train (Fig. 5*A*). Peak residual [Ca^{2+}] during the train in the absence of Ca^{2+} indicators was estimated as 3.8 μM by back-extrapolation (Fig. 5*D*; [3.1–5.5 μM], bootstrap 16–84% CI based on 40 experiments). The amplitude of 3.8 μM indicates that the Ca^{2+} transients from single APs (amplitude, 0.20 μM; Fig. 2*C*) summate markedly during short high-frequency bursts, resulting in high peak [Ca^{2+}] during trains. The estimates for τ, κ_E, and γ from train stimulation ($\tau = 86 \pm 26$ ms; $\kappa_E = 13 \pm 5$ and 17 ± 7 for A^{-1} and τ extrapolation, respectively; $\gamma = 210 \pm 27\ s^{-1}$; bootstrap SEM based on $n = 40$) were comparable to estimates from single APs (Fig. 2 and Fig. S3). However, analysis of stronger stimuli such as 100-ms depolarizations to 0 mV suggests a speeding of Ca^{2+} extrusion at higher [Ca^{2+}], as previously described (28). To investigate the contribution of mobile buffers, we added 100 μM of EGTA to the intracellular solution (Fig. S4*C*), which reduced the average peak amplitude by ∼30% ($P = 0.046$; Fig. S4*D*). In excellent agreement, adding 100 μM EGTA in simulations predicted a 31% reduction (Fig. S4 *E* and *F*). The fast Ca^{2+}-extrusion mechanisms in cMFBs prevent a summation of the slow component of residual Ca^{2+} transients caused by mobile buffers, which can evoke delayed release at some synapses (29, 30). These data demonstrate that endogenous mobile buffers reduce the buildup of residual Ca^{2+} during high-frequency bursts at cMFBs.

Modeling Ca^{2+} Transients in an Unperturbed Bouton. Because Ca^{2+} indicators perturb intracellular [Ca^{2+}], we used back-extrapolation to $\kappa_B = 0$ in Figs. 2 and 5. Extrapolation, however, does not address wash-out of mobile buffers. We therefore developed a detailed model to analyze residual Ca^{2+} (Fig. 6) and active zone Ca^{2+} (Fig. 7) of the unperturbed terminal. The model cMFB included the experimentally determined endogenous buffers (Figs. 2–5), Ca^{2+} current amplitude (8), and Ca^{2+} current facilitation (Fig. 5*B*). The predicted free [Ca^{2+}] was calculated from Ca^{2+} indicator occupancy, similarly as experimentally performed (*Materials and Methods*). Kinetic parameters of endogenous buffers were taken as experimentally determined values (see below). The remaining free parameters were optimized to reproduce the experimental data for single APs and trains of APs at 300 Hz with a single set of parameters (Fig. 6 *A* and *B*). With this model, we then analyzed Ca^{2+} transients in unperturbed boutons (without dyes, including mobile buffers), neglecting the possible influence of the intracellular solution on Ca^{2+}-extrusion mechanisms. Adding a mobile buffer (corresponding to 100 μM EGTA) markedly speeded Ca^{2+} transients to a decay time constant of ∼26 ms (Fig. 6 *C* and *D*). Thus, our data suggest that residual Ca^{2+} decays with a time constant of ∼26 ms and summates to a few micromolar during high-frequency firing in unperturbed boutons.

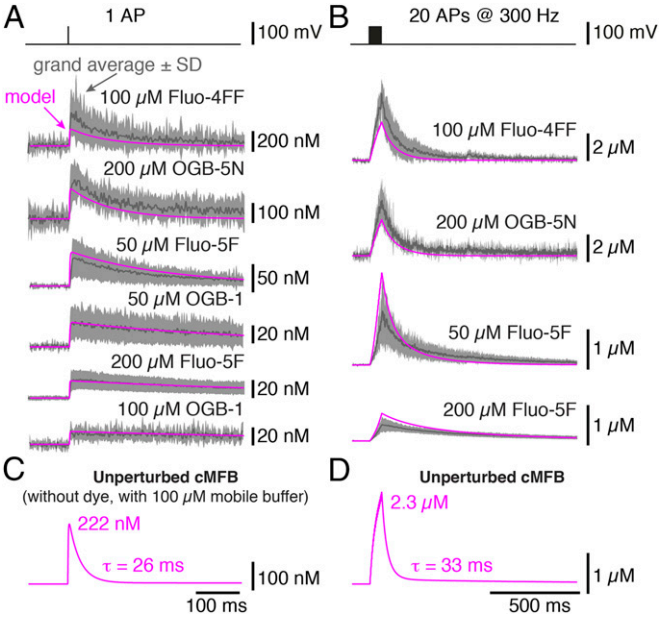

Fig. 6. Modeling Ca^{2+} transients in an unperturbed bouton. (*A* and *B*) Ca^{2+} transients elicited by a single AP (*A*) and a train of 20 APs at 300 Hz (*B*) recorded with different dyes superimposed with the corresponding model prediction (magenta). Bold lines are grand averages; gray shaded areas represent ±SD. The model was optimized to best reproduce all traces with a single set of parameters. (*C* and *D*) Simulation of a Ca^{2+} transient in response to a single AP (*C*) and a train of 20 APs at 300 Hz (*D*) at an unperturbed bouton (containing 100 μM of mobile buffer and no indicator dye).

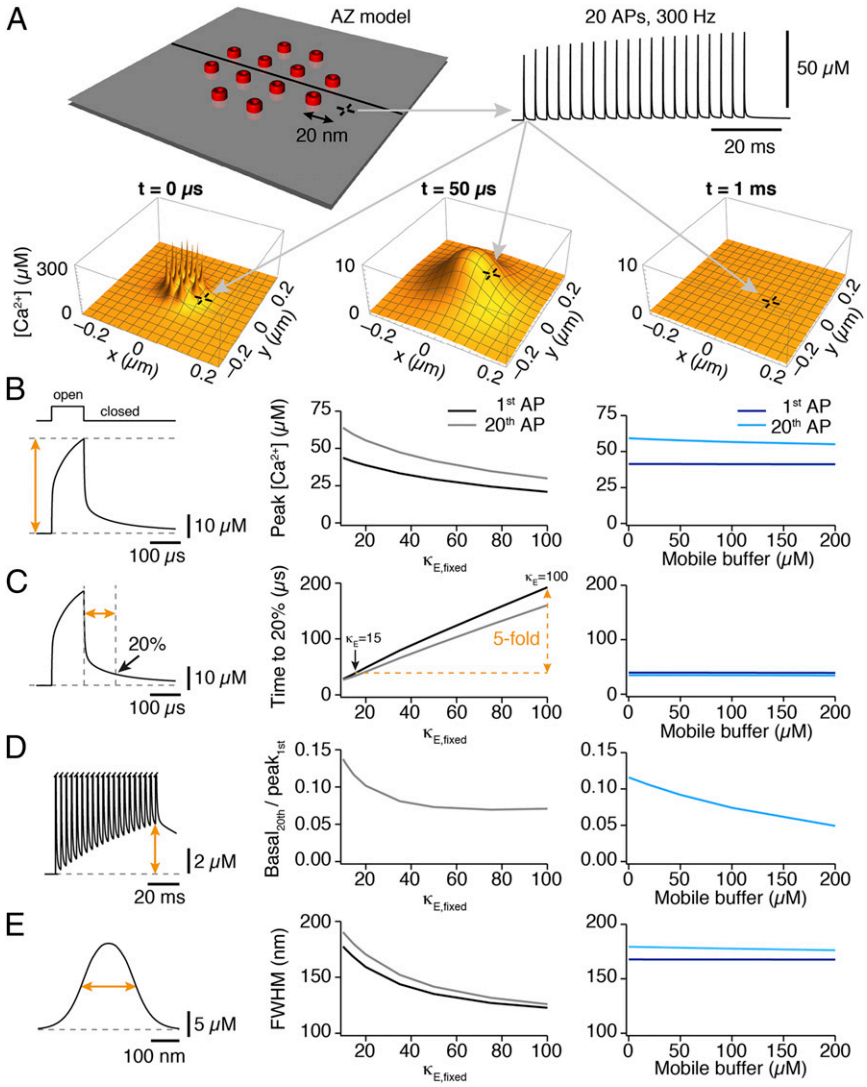

Fig. 7. Weak endogenous fixed buffers accelerate active zone Ca^{2+} signaling. (*A*) Visualization of the active zone model. The active zone contained 12 Ca^{2+} channels (red) spaced at 30 nm. The model simulated the influx, 3D buffered diffusion, and extrusion of Ca^{2+}. For one point at a distance of 20 nm from the channel (cross), the $[Ca^{2+}]$ is shown during a train of 20 APs at 300 Hz (*Upper Right*). Note that the increase in peak amplitude is mainly due to the implemented Ca^{2+} current facilitation (Fig. 5 *A* and *B*). The collapse of the free $[Ca^{2+}]$ microdomain is illustrated for three time points after the first AP ($t = 0$ μs, 50 μs, and 1 ms; end of the AP defined as $t = 0$). Within 50 μs, the Ca^{2+} domains of individual Ca^{2+} channels collapsed to a microdomain Ca^{2+} signal, which itself collapsed within 1 ms. (*B*) Peak amplitude of local $[Ca^{2+}]$ at a distance of 20 nm from the Ca^{2+} channel during the 1st and 20th AP at 300 Hz was reduced by increasing $\kappa_{E,fixed}$ (light and dark gray), but remained unaltered by increasing the concentration of mobile buffer (light and dark blue). The Ca^{2+} channel opening and the resulting local $[Ca^{2+}]$ are illustrated on the left. (*C*) Active zone Ca^{2+} clearance (defined as the time until the local $[Ca^{2+}]$ at 20 nm distance from the Ca^{2+} channel reaches 20% of its peak amplitude) was considerably slowed by increasing $\kappa_{E,fixed}$, being approximately fivefold longer for $\kappa_{E,fixed} = 100$ than for $\kappa_{E,fixed} = 15$. Active zone Ca^{2+} clearance was independent of the amount of mobile buffer between 0 and 200 μM. (*D*) Relative Ca^{2+} buildup during repetitive firing (defined as the $[Ca^{2+}]$ before the 20th AP normalized to the peak $[Ca^{2+}]$ of the 1st AP) was reduced by increasing $\kappa_{E,fixed}$ up to 50 and by increasing concentrations of mobile buffer. (*E*) The spatial extent of active zone Ca^{2+} (defined as FWHM of a line profile through the center of the active zone 50 μs after the AP) decreased with increasing $\kappa_{E,fixed}$ but was unaffected by the amount of mobile buffer.

Weak Endogenous Fixed Buffers Accelerate Active Zone Ca^{2+} Signaling. How can cMFBs sustain synchronous vesicular release despite the substantial summation of residual Ca^{2+} during high-frequency firing? To address this question, we investigated the spatiotemporal dynamics of Ca^{2+} at the active zone and the influence of endogenous fixed and mobile buffers. We simulated active zone Ca^{2+} diffusion and buffering based on the model established above (*Materials and Methods*) during a train of 20 APs at 300 Hz. The local $[Ca^{2+}]$ of the 1st and 20th AP was analyzed at a distance of 20 nm from a channel (Fig. 7*A*). We focused our analysis on four functionally important parameters: First, the local peak $[Ca^{2+}]$ of the 1st and 20th AP, which was markedly decreased with increasing $\kappa_{E,fixed}$, but increasing the slow mobile buffer concentration (0–200 μM), had little effect (Fig. 7*B*). Second, the local Ca^{2+} clearance was defined as the time needed for $[Ca^{2+}]$ to decrease to 20% of the peak during the AP. Clearance was much faster for lower $\kappa_{E,fixed}$ (fivefold acceleration with $\kappa_{E,fixed}$ of 15 compared with 100), but depended little on the amount of mobile buffer (Fig. 7*C*). Third, the relative Ca^{2+} buildup during repetitive firing was defined as the $[Ca^{2+}]$ before the 20th AP normalized to the peak $[Ca^{2+}]$ of the 1st AP. Increasing $\kappa_{E,fixed}$ up to 50 reduced the relative buildup by a factor of ~2, and increasing $\kappa_{E,fixed}$ above 50 had no further effect. Increasing the mobile buffer concentration up to 200 μM reduced the relative buildup by a factor of ~3 (Fig. 7*D*). Fourth, the spatial extent of active zone Ca^{2+} was measured as full-width at half-maximum (FWHM) of a line profile through the center of the active zone 50 μs after the AP. FWHM was markedly enlarged with lower $\kappa_{E,fixed}$, but remained unaltered by changing the amount of mobile buffer (Fig. 7*E*), consistent with previous analytical calculations of the length constant (mean distance a Ca^{2+} ion diffuses before being captured by a buffer molecule) (31, 32). To investigate the sensitivity of our results on the parameters of the model, we varied these parameters and obtained similar results to those shown in Fig. 7, revealing the robustness of our modeling approach (*Materials and Methods*).

These data demonstrate that a low $\kappa_{E,fixed}$ enables active zone Ca^{2+} signals with high amplitude, large spatial extent, and rapid decay. Furthermore, a high concentration of mobile buffer reduces the buildup of Ca^{2+} between APs. Thus, fixed endogenous buffers with low affinity and low Ca^{2+}-binding ratio in combination with mobile buffers with high affinity seem ideally suited to speed active zone Ca^{2+} clearance and thus enable synchronous and reliable high-frequency transmission.

Ca^{2+} Signals at Different Distances from Active Zones. The rapid clearance of Ca^{2+} from the active zone suggests that during an AP, Ca^{2+} rapidly diffuses from active zones into the center of the presynaptic terminal. One might therefore expect that $[Ca^{2+}]$ rises slightly slower at the center of the cMFB than at the edge

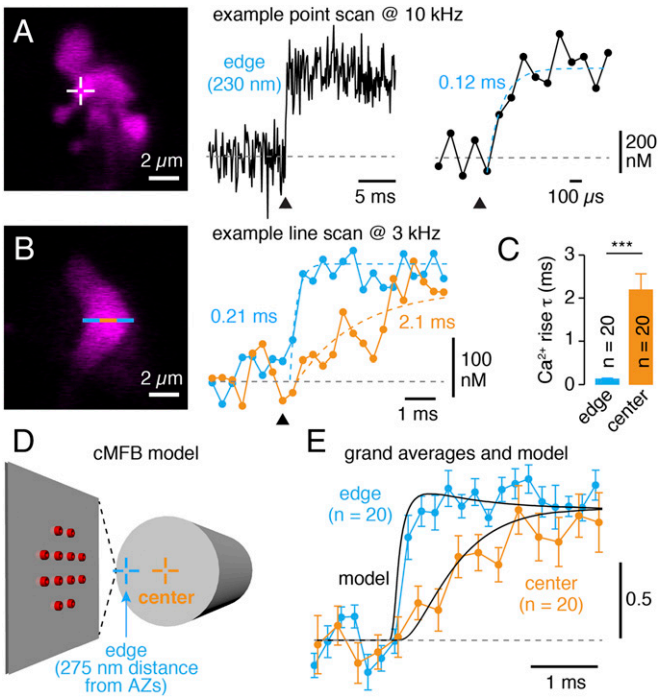

Fig. 8. Ca^{2+} signals at different distances from active zones. (*A*) Example of a two-photon point scan (sampling rate, 10 kHz) close to the edge of a cMFB (230 nm). (*Left*) Two-photon image of bouton filled with 10 μM Atto594 and 200 μM OGB-5N. (*Center*) In response to an AP (arrowhead), a rapid rise of [Ca^{2+}] was observed. Unfiltered data trace; average of 34 traces. (*Right*) Rise of [Ca^{2+}] on expanded time scale superimposed with exponential fit (blue dotted line; time constant, 120 μs). (*B*) Example of two-photon line scan at 3-kHz resolution at the center and close to the edge of boutons. (*Left*) Two-photon image of a bouton filled with 10 μM Atto594 and 200 μM OGB-5N. (*Right*) In response to an AP (arrowhead), a faster rise of [Ca^{2+}] was observed close to the edge of the cMFB compared with the center. Average of 49 traces each; blue and orange dotted lines are exponential fits, time constants are indicated. (*C*) Average rise time constants (n = 20 each, $P < 0.00001$, unpaired t test). (*D*) Illustration of the cylindrical cMFB model. Ca^{2+} influx occurs at the surface of the cylinder, where active zones are located. (*E*) Grand averages of subbouton Ca^{2+} signals superimposed with the model predictions at two distances from the surface (edge, 275 nm; center, 0.9 μm) as illustrated in *D*. Data were peak normalized and binned with 0.2-ms (edge, n = 20) or 0.3-ms bin duration (center, n = 20); error bars represent SEM.

where active zones are located. To experimentally confirm this prediction, we performed measurements with the low-affinity dye OGB-5N and with increased spatial and temporal resolution. High-resolution point and line measurements (5- to 10- and 1- to 3-kHz sampling rate, respectively) revealed extremely rapid rise kinetics at the edge of cMFBs (0.143 ± 0.01 ms; n = 20; average distance to edge, 278 ± 42 nm), significantly faster than at the center (2.20 ± 0.37 ms, n = 20; $P < 0.001$, unpaired t test; Fig. 8 *A*–*C*). The resolved difference in Ca^{2+} kinetics is most likely caused by equilibration of Ca^{2+} microdomains within cMFBs. In our cMFB model, the Ca^{2+} influx is restricted to the surface of the cylinder, representing the ∼300 active zones at the surface of cMFBs (Fig. 8*D*). The model nicely reproduced the high-resolution Ca^{2+} measurements (Fig. 8*E*), providing an independent validation of our modeling approach.

From the high-resolution data at the edge of cMFBs, we additionally determined limits for the binding kinetics of the endogenous fixed buffers. The analyses (Fig. S5) revealed that k_{off} must be >10,000 s^{-1}, K_D > 20 μM, and $k_{on} < 6 \times 10^9$ $s^{-1} \cdot M^{-1}$, which is close to the upper diffusion limit. Our boundaries for k_{off} and K_D are similar to previous approximations at the calyx of Held presynaptic terminal (20, 33) and at chromaffin cells (34) and indicate that the endogenous fixed buffers at cMFBs are of low affinity with fast binding kinetics.

Weak Endogenous Fixed Buffers Enable Highly Synchronous Release. To investigate whether the rapid clearance of Ca^{2+} from the active zone caused by weak endogenous fixed buffers promotes synchronous neurotransmitter release, we simulated the time course of release rate for a single AP (Fig. 9*A*). The duration and amplitude of the vesicular release rate were highly dependent on $\kappa_{E,fixed}$. With $\kappa_{E,fixed}$ = 15, the FWHM of the release rate was 114 μs, similar to previously measured values (27). With $\kappa_{E,fixed}$ = 100, however, the FWHM was prolonged 2.8-fold (Fig. 9*B*). These results had little dependence on the implementation of the release scheme (Fig. S6). Thus, the strength of endogenous fixed Ca^{2+} buffers limits the synchronicity of release.

Discussion

In this study, we identified the mechanisms controlling the speed of active zone Ca^{2+} signaling using quantitative two-photon Ca^{2+} imaging with submillisecond temporal and subbouton spatial resolution at central presynaptic terminals. We found a surprisingly low Ca^{2+}-binding ratio of endogenous fixed buffers. Our experimentally constrained model revealed that such weak Ca^{2+} buffering enables rapid diffusional removal of Ca^{2+} from the active zone. Thus, our study provides a framework of presynaptic Ca^{2+} signaling explaining how central synapses can sustain fast and synchronous neurotransmitter release.

Low Ca^{2+}-Binding Ratio. Dissection of fixed and mobile Ca^{2+} buffers requires efficient control of the cytosolic solution. This procedure has been performed at few preparations such as chromaffin cells (23, 35) and dendrites dialyzed via somatic recordings (18, 36–39). Previous studies investigating κ_E at presynaptic terminals provided estimates ranging from ∼20 at hippocampal mossy fiber boutons (15), ∼56 at boutons of cerebellar granule cells (21), and ∼140 at boutons of layer 2/3 neocortical pyramidal cells (22), to up to ∼1,000 at the crayfish neuromuscular junction (40). Due to somatic or axonal loading in these studies, however, mobile buffers might have contributed,

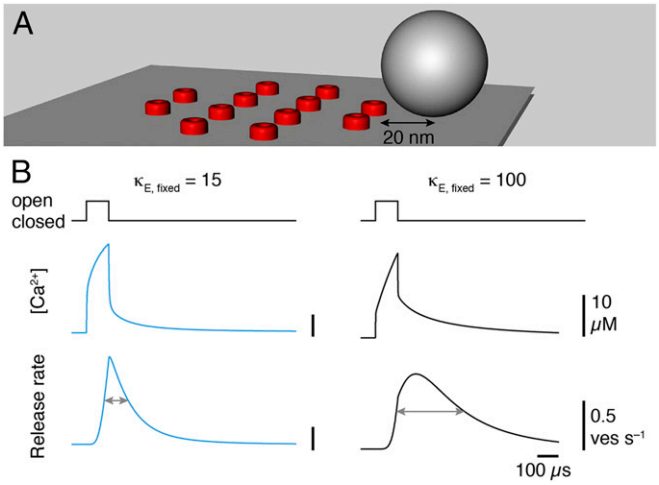

Fig. 9. Weak endogenous fixed buffers enable highly synchronous release. (*A*) Visualization of the active zone model (Fig. 7). Ca^{2+} channel to vesicle coupling distance was 20 nm. The release scheme was based on ref. 75; see Fig. S6 for details. (*B*) Comparison of the local [Ca^{2+}] at the position of the vesicle (*Middle*) and release rate (*Bottom*) for a single AP (Ca^{2+} channel opening illustrated at *Top*) with different binding ratios of fixed buffer ($\kappa_{E,fixed}$ = 15 and 100). Low $\kappa_{E,fixed}$ leads to highly synchronous release.

leading either to overestimation of $\kappa_{E,fixed}$ or, as demonstrated in Fig. 3*G*, to underestimation of $\kappa_{E,fixed}$. To our knowledge, a rigorous dissection of mobile and fixed buffers at presynaptic terminals has only been possible at preloaded and whole-cell dialyzed calyx of Held synapses (9) and at somatically loaded presynaptic terminals of retinal bipolar cells (10). At the calyx of Held, values for $\kappa_{E,fixed}$ of ∼22 (25), ∼40 (14, 20), or ∼46 (41) have been determined. By systematic dialysis of cMFBs with Ca^{2+} indicators of different affinity, we demonstrate a Ca^{2+}-binding ratio of the fixed buffers of ∼15 (Fig. 2). Thus, our data show that $\kappa_{E,fixed}$ at cMFBs is lower than all previously determined values.

Because the estimate of $\kappa_{E,fixed}$ depends on correct quantification of $[Ca^{2+}]$, we used three independent quantification approaches: two-photon Ca^{2+} imaging with dual-indicator quantification based on intrabouton calibration; two-photon Ca^{2+} imaging with single-indicator quantification based on an independent calibration approach (Figs. S1 and S2); and ratiometric Ca^{2+} imaging with Fura-2 using UV-epifluorescence excitation. The three independent methods were in excellent agreement, demonstrating the reliability of our quantification.

In addition, our high-resolution experiments revealed that the endogenous fixed buffers have low affinity (K_D > 20 μM; Fig. S5), consistent with estimates at the calyx of Held (20, 33), indicating that fixed buffers are present at >300 μM concentration in cMFBs (calculated from κ_E = 15 and K_D > 20 μM; Fig. S5).

Mobile Ca^{2+} Buffers with Slow Binding Kinetics. By comparing remote and dialyzed boutons we demonstrate that—in addition to the background of fixed buffers—there is a small but substantial contribution of mobile Ca^{2+} buffers with slow, EGTA-like kinetics (Figs. 3 and 4). These high-affinity mobile buffers speed the decay of residual Ca^{2+} in cMFBs (Fig. 4) in a strikingly similar way to mobile buffers at the calyx of Held (9). In contrast, we found that mobile buffers had little impact on active zone Ca^{2+} clearance (see below). Simple calculation of the Ca^{2+}-binding ratio of mobile buffers ($\kappa_B = [B]/K_D$) results in ∼500. However, the concept of a binding ratio is only useful if Ca^{2+} and buffers are in kinetic equilibrium and if the equilibration time constant between slow buffers and Ca^{2+} is faster than the Ca^{2+}-extrusion rate (23). At cMFBs, though, extrusion and equilibration time constant are both in the range of 100 ms (Figs. 2 and 5).

The molecular identity of endogenous mobile buffers is unknown at cMFBs, but Ca^{2+}-binding proteins including parvalbumin, calretinin, and calbindin-D28k are obvious candidates (3, 42). Kinetically, parvalbumin seems a likely candidate for a slow buffer (9, 43). However, we found very weak expression levels of parvalbumin, calretinin, and calbindin-D28k assessed with immunohistochemistry in cMFBs, indicating that none of these proteins is a dominant Ca^{2+} buffer in cMFBs. Because Ca^{2+} transients were very similar in patched boutons in the presence of EGTA and in remote boutons in the presence of mobile buffers (Fig. 4), we used a mobile buffer with kinetics of EGTA in our simulations and did not implement any cooperativity (44, 45).

Speeding Active Zone Ca^{2+} Signaling. We show that a low Ca^{2+}-binding ratio of endogenous fixed buffers is essential for Ca^{2+} microdomains with high amplitudes, large spatial extent, and rapid clearance (Fig. 7). Although one could assume that a high $\kappa_{E,fixed}$ has the potential to efficiently remove Ca^{2+} from the active zone, our results show the opposite, namely that a low $\kappa_{E,fixed}$ speeds active zone Ca^{2+} clearance (Fig. 7). This finding can be explained by the acceleration of the apparent Ca^{2+} diffusion by reduced fixed buffers (46) and, intuitively, by less unbinding of Ca^{2+} from the fixed buffers in-between APs.

In addition, slow mobile buffers help to prevent facilitation of intracellular $[Ca^{2+}]$ during high-frequency firing but have little impact on active zone Ca^{2+} signals at cMFBs (Fig. 7 and Fig. S4). In contrast, mobile buffers seem to influence active zone Ca^{2+} signals at hippocampal mossy fiber boutons (47) and ribbon-type synapses (10, 48, 49). In these preparations, however, the mobile buffers have faster kinetics and/or the Ca^{2+} channel to vesicle coupling is less tight compared with cMFBs (8). Under these conditions, binding to the slow buffer and an acceleration of the apparent Ca^{2+} diffusion by mobile buffers (37, 46, 50) are expected to impact active zone Ca^{2+} signals. Furthermore, our data argue against substantial saturation of mobile buffers causing facilitation of release (38, 51). The low affinity of fixed buffers at cMFBs (Fig. S5) also prevents substantial saturation, which would allow slow buffers to impact local Ca^{2+} signals (43).

Thus, our results establish that active zone Ca^{2+} signaling is mainly accelerated by the lack of a large amount of fixed buffers allowing rapid diffusional collapse of local Ca^{2+} signals and by mobile buffers with slow kinetics that bind Ca^{2+} during fast repetitive firing. This concept of active zone Ca^{2+} signaling is consistent with the low $\kappa_{E,fixed}$ found in cMFBs and the synchronous release of cMFBs during high-frequency transmission (8). The previously determined larger presynaptic $\kappa_{E,fixed}$ and the slower firing regimes of the respective synapses corroborate the concept that the strength of endogenous fixed buffers limits the maximum synchronous transmission frequency.

Resolving Intrabouton Ca^{2+} Diffusion During Single APs. In this study, we resolved local Ca^{2+} signals during the equilibration of microdomain Ca^{2+} at a mammalian central synapse (Fig. 8). Recently, local Ca^{2+} signals at synaptic and nonsynaptic regions were resolved with different rise time and initial amplitude at the calyx of Held synapse (20). Furthermore, local Ca^{2+} signals with long-lasting differences in amplitude were recorded at hippocampal mossy fiber boutons (52). In contrast, we measured complete Ca^{2+} equilibration within the first few milliseconds of a single AP. The fast rise time (∼140 μs) argues that our local Ca^{2+} signals were recorded very close to the Ca^{2+} entry site. The small size of cMFBs with active zones that are small (diameter, 160 nm) (53) and closely spaced (∼400 nm) (54) can explain the rapid equilibration (model prediction in Fig. 8*E*).

Experimental high-resolution analysis of intrabouton Ca^{2+} diffusion is essential to understand Ca^{2+} dynamics at the active zone and to constrain computer simulations. Previously, comparable analyses of local Ca^{2+} signals have also been performed at neuromuscular junctions (2, 55), cerebellar synaptosomes (56), chromaffin cells (57), and inner hair cells (58). Our results at bona fide central synapses are consistent with the previous studies and extend our understanding of microdomain signaling by elucidating the differential role of endogenous fixed and mobile buffers for active zone Ca^{2+}-signals.

Conclusion

The fixed endogenous Ca^{2+} buffers of cerebellar mossy fiber boutons are of low affinity and have a very low binding capacity. The buffering properties of cMFBs are ideal for rapid clearance of Ca^{2+} from the active zone, which allows synchronous release at high repetition rates. These data pinpoint the mechanisms allowing highly synchronous, fast neurotransmitter release at central presynaptic terminals.

Materials and Methods

Electrophysiology. Cerebellar slices were prepared from P21–P61 CD-1, or C57BL/6 mice of either sex. Animals were treated in accordance with the German Protection of Animals Act and with the guidelines for the welfare of experimental animals issued by the European Communities Council Directive. Mice were anesthetized with isoflurane and killed by rapid decapitation; the cerebellar vermis was quickly removed and mounted in a chamber filled with chilled extracellular solution. Parasagittal 300-μm-thick slices were cut using a Leica VT1200 microtome (Leica Microsystems), transferred to an incubation chamber at 35 °C for ∼30 min, and then stored at room temperature until use. The extracellular solution for slice cutting, storage, and experiments contained (in mM) the following: NaCl 125, $NaHCO_3$ 25, glucose 20, KCl 2.5, $CaCl_2$ 2, NaH_2PO_4 1.25, $MgCl_2$ 1 (310 mOsm,

pH 7.3 when bubbled with Carbogen [5% (vol/vol) O_2/95% (vol/vol) CO_2]). Presynaptic patch-pipettes were pulled to open-tip resistances of 6–16 MΩ (when filled with intracellular solution) from borosilicate glass (Science Products) using a DMZ Puller (Zeitz-Instruments). The intracellular solution contained (in mM) the following: K-Gluconate 150, NaCl 10, K-Hepes 10, Mg-ATP 3, and Na-GTP 0.3 (pH adjusted to 7.3 using KOH). Atto594 (10–20 μM) and one of the following Ca^{2+}-sensitive dyes were added to the intracellular solution: OGB-1 (50 or 100 μM), Fluo-5F (50 or 200 μM), Fluo-4FF (100 μM), or OGB-5N (200 μM). Experiments were performed at 34–37 °C. We purchased Atto594 from Atto-Tec, Ca^{2+}-sensitive fluorophores from Life Technologies, and all other chemicals from Sigma-Aldrich.

Cerebellar mossy fiber boutons were visualized with oblique illumination and infrared optics. Whole-cell patch-clamp recordings from cMFBs were made using a HEKA EPC10/2 amplifier (HEKA Elektronik). Presynaptic cMFBs were identified as previously described (8). Measurements were corrected for a liquid junction potential of +13 mV. Series resistance was typically <40 MΩ. APs were evoked in current-clamp mode by brief current pulses (amplitude 50–500 pA; duration 1–3 ms). For train stimulations (20 stimuli at a frequency of 300 Hz), brief depolarizations (0 mV, 200 μs) were applied in voltage-clamp mode. Ca^{2+} transients recorded in response to current injections (current-clamp) or short depolarizations (voltage-clamp) did not differ in amplitude or decay time constant (Fig. S1*C*). In voltage-clamp experiments, the holding potential was −80 mV.

Quantitative Two-Photon Ca^{2+} Imaging. Two-photon Ca^{2+} imaging was performed with a Femto2D laser-scanning microscope (Femtonics) equipped with a pulsed Ti:Sapphire laser (MaiTai, SpectraPhysics) tuned to 810 nm, a 60×/1.0 NA objective (Olympus) or 100×/1.1 NA objective (Nikon), and a 1.4 NA oil-immersion condenser (Olympus). Data were acquired in line scan mode, typically at a 1-kHz sampling rate. In a subset of experiments, we performed line- and point-scan measurements with a sampling rate of 3–10 kHz (Figs. 5*A* and 8 and Figs. S4 and S5). Background was measured outside of boutons in a neighboring area and subtracted. Imaging data were acquired and processed using Mes software (Femtonics).

We calculated the ratio (R) of green-over-red fluorescence to quantify intracellular $[Ca^{2+}]$ with Ca^{2+} indicators of different affinity. Using green and red indicators, $[Ca^{2+}]$ can be calculated as (13)

$$\left[Ca^{2+}\right] = K_D \frac{R - R_{min}}{R_{max} - R}. \quad [1]$$

Minimum (R_{min}) and maximum (R_{max}) fluorescence ratios were determined with 10 mM EGTA or 10 mM $CaCl_2$ in the intracellular solution, respectively. We performed these measurements in situ, i.e., in cMFBs or cerebellar granule cells to account for possible different dye properties in cytosol (17). Details of the calibration are described in *SI Materials and Methods*. For the high-affinity dye OGB-1, we also compared single- and dual-indicator quantification methods, which gave very similar results (*SI Materials and Methods* and Figs. S1*B* and S3*A*).

The decay of the Ca^{2+} concentration (C) was fit with an exponential function

$$C(t) = A_0 + A\, e^{(-t/\tau)}, \quad [2]$$

where A_0 was constrained to the baseline level calculated for 20–90 ms before stimulation. For display purposes, Ca^{2+} transients in the figures were digitally filtered using Igor Pro software (Wavemetrics; −3-dB filter cutoff frequency, 170 Hz) unless stated otherwise (Figs. 2*A*, 5*A*, and 8 and Fig. S5).

The two-photon signal is a convolution of the imaged structure and the microscope's point-spread function. Typical dimensions of two-photon point-spread functions are <1 μm radially and <2 μm axially (59). Because most cMFBs have a diameter >3 μm (54), the heterogeneous fluorescence signal within boutons (Fig. 8) cannot be explained by artifacts due to partial overlap of the point-spread function with boutons but rather represents kinetic differences of the intrabouton $[Ca^{2+}]$.

Ratiometric Fura-2 Ca^{2+} Imaging. In addition, presynaptic Ca^{2+} transients were recorded using Fura-2 (100 μM) and a Ca^{2+}-imaging system (TILL-Photonics) with an excitation light source (Polychrome V) coupled to the epifluorescence port of the microscope (FN-1 with 100×/1.1 NA objective; Nikon) via a light guide, following previous descriptions (18, 33, 60). Fluorescence was measured with a back-illuminated electron-multiplying frame-transfer charge coupled device camera (iXon DU897; Andor Technology). Fura-2 fluorescence at both 350 and 380 nm was sampled every 10–30 ms; camera binning was 8 × 8. Background was measured in an area close to the patched bouton and subtracted. In these experiments, $[Ca^{2+}]$ was calculated as previously described (18, 33, 60)

$$\left[Ca^{2+}\right] = K_{eff} \frac{R - R_{min}}{R_{max} - R}, \quad [3]$$

and the effective dissociation constant (K_{eff}) as

$$K_{eff} = K_D \frac{R_{max} + \alpha}{R_{min} + \alpha}, \quad [4]$$

where α is the isocoefficient, K_D the dissociation constant of Fura-2 (0.286 μM) (36), and $R = F_1/F_2$, where F_1 and F_2 are the background-subtracted fluorescence intensities at 350 and 380 nm, respectively. For Fura-2 experiments, R_{max} and R_{min} were measured in cells using 10 mM $CaCl_2$ or 10 mM EGTA, respectively. The isocoefficient α was determined by adjusting α to obtain a Ca^{2+} independent sum of $F_1 + \alpha F_2$ as previously described (35), resulting in a value of ∼0.05.

Estimation of Endogenous Buffer Ratio. We used the "added buffer method" to estimate the endogenous buffering capacity at cMFBs (17). The incremental Ca^{2+}-binding ratio of exogenous buffers (κ_B) was calculated as (14)

$$\kappa_B = \frac{[B]K_D}{\left([Ca^{2+}]_{rest} + K_D\right)\left([Ca^{2+}]_{peak} + K_D\right)}, \quad [5]$$

where [B] is the concentration of the exogenous buffer, $[Ca^{2+}]_{rest}$ is the free Ca^{2+} concentration under resting conditions, and $[Ca^{2+}]_{peak} = [Ca^{2+}]_{rest} + \Delta[Ca^{2+}]_{AP}$, where $\Delta[Ca^{2+}]_{AP}$ is the baseline subtracted amplitude of the AP-evoked Ca^{2+} transient. According to the single-compartment model, the decay time constant (τ) and the inverse of the amplitude (A^{-1}) of the Ca^{2+} transient depend linearly on κ_B of the added buffer (4, 36)

$$A = \frac{Q_{Ca}/(2\,FV)}{(1 + \kappa_B + \kappa_E)}, \quad [6]$$

$$\tau = \frac{(1 + \kappa_B + \kappa_E)}{\gamma}, \quad [7]$$

where Q_{Ca} is the charge flowing into the presynaptic terminal, F is the Faraday constant, V is the accessible volume of the terminal, and γ is the Ca^{2+}-extrusion rate. We plotted A^{-1} and τ obtained from experiments vs. κ_B. Extrapolation of the linear regression line to $\kappa_B = 0$ yields an estimate of the Ca^{2+} transient without added exogenous buffer; the *x* axis intercept equals $-(1 + \kappa_E)$ (4). Gluconate and nucleotides in the intracellular solution contribute an additional κ of ∼4.5 (61). We therefore added 4.5 to all κ_B values of the intracellular solutions in our analysis.

Confidence intervals of κ_E, A, τ, and γ estimates by back-extrapolation (Figs. 2 and 5) were determined by bootstrap procedures (62) implemented in Mathematica 10. An artificial dataset was taken from the original dataset, with replacement. Ten thousand datasets were generated and analyzed as the original dataset.

Dye Loading in Remote Boutons. CMFBs were filled with 10–20 μM Atto594 for visualization and 200 μM Fluo-5F to record Ca^{2+} transients at remote boutons. Immediately after gaining whole-cell access, the red channel was used to locate a remote bouton along the same axon. Ca^{2+} transients were subsequently recorded at this remote bouton with APs evoked in current-clamp mode every 15–30 s. To describe the diffusion of dyes and endogenous mobile buffers, the mossy fiber axon was approximated by a semi-infinite cylinder. Consequently, the intensity of fluorescence reflecting the increasing dye concentration over time was fit using the following equation (63):

$$F(t) = F_0\, erfc\left(\frac{x}{2\sqrt{D\,t}}\right), \quad [8]$$

where F_0 denotes the fluorescence at maximum dye concentration during steady state, x is the distance (constrained to the measured distance between patched and remote bouton in every experiment), D is the diffusion coefficient of the dye, and *erfc* is the complementary error function given as

$$erfc(z) = \frac{2}{\sqrt{\pi}} \int_z^{\infty} e^{-y^2}\, dy. \quad [9]$$

Red and green fluorescence (i.e., 90-ms baseline before AP) was plotted vs. dye-loading time (Fig. 3*C*) and fit using Eq. **8**.

In all experiments, the resulting apparent diffusion coefficients were higher for Atto594 than for Fluo-5F (35.4 ± 7.0 and 20.5 ± 4.0 $\mu m^2 \cdot s^{-1}$, respectively). Therefore, we determined the concentration of the dyes separately from the fit with Eq. **8**, referred to as [Atto] and [Fluo] in the following. For each time point of the dye loading, we calculated a corrected green-over-red ratio R* as

$$R^* = R\frac{[\mathrm{Atto}]/[\mathrm{Atto}]_{\mathrm{pipette}}}{[\mathrm{Fluo}]/[\mathrm{Fluo}]_{\mathrm{pipette}}}, \quad [10]$$

where $[\mathrm{Atto}]_{\mathrm{pipette}}$ and $[\mathrm{Fluo}]_{\mathrm{pipette}}$ are the red and green dye concentrations in the pipette, respectively. κ_B was determined with Eq. **5** using the [Fluo] and Ca^{2+} transient amplitude. At the end of dye loading experiments, Ca^{2+} transients in remote boutons had a slightly faster decay and higher amplitude than in patched boutons (τ: 494 ± 55 vs. 681 ± 47 ms, $P = 0.02$; amplitude: 24.3 ± 3.4 vs. 19.7 ± 1.1 nM, $P = 0.1$; $n = 26$ and 57, respectively). This difference is consistent with lower dye concentrations in remote compared with patched boutons, as expected from Eq. **8** and the limited time course of these experiments. In our analysis, we did not correct for differences in z-depth between patched and remote boutons, as fluorescence ratios were <20% different up to 100-μm depth measured with sealed pipettes.

Ca^{2+} Current Recordings. In some experiments (Fig. 5 *A* and *B*), we pharmacologically isolated presynaptic Ca^{2+} currents during cMFB whole-cell patch-clamp recordings as previously described (8). Ca^{2+} currents were elicited by step depolarizations of 200-μs duration from −80 to 0 mV. Ca^{2+} currents were corrected for leak and capacitance currents using the P/4 method. In these experiments, the extracellular solution consisted of (in mM) the following: NaCl 105, KCl 2.5, NaH_2PO_4 1.25, $NaHCO_3$ 25, glucose 25, $CaCl_2$ 2, $MgCl_2$ 1, TTX 0.001, 4-AP 5, and TEA 20. The presynaptic patch pipette contained (in mM) the following: CsCl 135, TEA-Cl 20, MgATP 4, NaGTP 0.3, Na_2phosphocreatine 5, Hepes 10, and EGTA 0.2.

Modeling of Spatiotemporal Ca^{2+} Diffusion and Buffering. The model simulated the time course of Ca^{2+} influx and buffered diffusion in a cMFB, using a finite-difference scheme (51, 64–66). Previous electrophysiological experiments (8) and our Ca^{2+}-imaging measurements constrained key parameters of the model (Table S1). Simulations were implemented in CalC 7.7.4 (67); further evaluations were performed with Wolfram Mathematica 10. All calculations were executed on a MacBook Pro computer with 2.7-GHz Intel Core i7 processor and 16-GB RAM operating on Mac OS X 10.8.

When simulating Ca^{2+} dynamics in the whole cMFB (Figs. 6 and 8), we assumed a cylindrical morphology, 1.8 μm in diameter and 24.8 μm in length, to reproduce the Ca^{2+} transients recorded with the various dyes (Fig. 6) and the diffusional properties within cMFBs (Fig. 8). Grid size of the model was set to 20 points in radial and longitudinal dimensions (increasing grid size did not change the results). The AP-evoked Ca^{2+} current influx at the surface of the cylinder was approximated by a Gaussian of 99-μs FWHM and 543-pA peak amplitude (8). The simulations included fixed endogenous buffers, ATP, gluconate (Table S1), and the following Ca^{2+} extrusion pump mechanism, which was implemented with the Ca^{2+} flux, J, defined as

$$J = -\gamma\left([Ca^{2+}] - [Ca^{2+}]_{\mathrm{rest}}\right) - V_{\max}\left(\frac{[Ca^{2+}]^n}{[Ca^{2+}]^n + K_D^n} - \frac{[Ca^{2+}]^n_{\mathrm{rest}}}{[Ca^{2+}]^n_{\mathrm{rest}} + K_D^n}\right), \quad [11]$$

where $\gamma = 0.14\ \mu m \cdot ms^{-1}$, $V_{max} = 0.25\ \mu M \cdot \mu m \cdot ms^{-1}$, n = 2.5, and $K_D = 3.7\ \mu M$. J has units of $\mu M \cdot \mu m \cdot ms^{-1} = 10^{-6}\ mol \cdot m^{-2} \cdot s^{-1}$. The second nonlinear component of the definition describes the speeding of Ca^{2+} extrusion at higher $[Ca^{2+}]$, e.g., during 100-ms depolarization to 0 mV, and is based on previous analyses of Ca^{2+} extrusion mechanisms (28). The parameters V_{max}, n, and K_D were adjusted to reproduce the measured Ca^{2+} transients elicited by single APs and trains of APs (Fig. 6 *A* and *B*). The model did not include an axon, but diffusion of Ca^{2+} into the mossy fiber axon would be pooled in the implemented extrusion mechanism.

When modeling Ca^{2+} dynamics on a fine spatial scale at a single active zone (Fig. 7), we represented the active zone with a rectangular box (65). To reduce simulation time we took advantage of the assumed symmetry with respect to two perpendicular planes and considered only a quarter of this volume comprising three Ca^{2+} channels. The *x-y* dimensions were 0.23 μm (corresponding to half of the distance between neighboring active zones) (54), and the *z* dimension was 1.0 μm. The active zone model had a spatial grid of 50 × 50 × 30 points (*x,y,z*), with slight stretching implemented in the corner containing the channels (51). Boundary conditions on all side surfaces were set to be no flux and on the top surface to Dirichlet (boundary value clamped to background $[Ca^{2+}]$). On the bottom surface (Ca^{2+} channel plane), the Ca^{2+} extrusion pump (Eq. **11**) was added. Parameters used in the simulations are given in Table S1. Binding rates of EGTA were taken from ref. 68, which were estimated at physiological temperature and pH 7.3. The resulting K_D was 200 nM, which is similar to commonly used parameters estimated at room temperature (69, 70). To analyze unperturbed active zone Ca^{2+} signaling, active zone simulations included ATP and fixed and mobile buffers as stated (Fig. 7) without gluconate.

Per active zone, 12 open Ca^{2+} channels with a single channel current of 0.15 pA (71) and a duration of 105 μs (8) were assumed. The number of Ca^{2+} channels is thus constrained by the measured Ca^{2+} influx per AP in cMFBs (macroscopic Gaussian-like Ca^{2+} current with half-duration of 99 μs, and peak amplitude of 543 pA) (8), assuming 300 active zones per cMFB (54). The distance between Ca^{2+} channels was 30 nm, consistent with freeze-fracture replica labeling (8). Channel open times were fixed for all channels, and single channel open probability was set to 1. Stochastic implementation of an open probability < 1 (71) would result in a larger number of channels per simulated active zone due to the constraint by the measured Ca^{2+} influx. A larger number would increase the net distance between open channels, which was addressed in the following sensitivity analysis.

To investigate the sensitivity of simulations on model parameters, we systematically varied the number of open Ca^{2+} channels (range, 4–36), single channel conductance (range, 0.05–0.4 pA), distance between Ca^{2+} channels (range, 10–60 nm), and the distance of the position where the local Ca^{2+} concentration was sampled to the nearest Ca^{2+} channel (range, 10–60 nm). Furthermore, the number of *x-y* grid points (range, 10–80) and CalC accuracy parameter (range, 10^{-1}–10^{-7}) were varied. As expected from previous studies investigating the impact of Ca^{2+} distribution on synaptic release (20, 65, 66, 72–74), the peak local $[Ca^{2+}]$ was different when we varied the model parameters (range, 12–122 μM). However, the main finding of this study—the speeding of active zone Ca^{2+} signaling with low $\kappa_{E,fixed}$—was very robust with all tested parameters (fold-change of clearance time for $\kappa_{E,fixed}$ of 15 and 100 as indicated in Fig. 7*C* ranged from 3.2 to 8.9).

Modeling of the Release Time Course. To simulate the time course of vesicular release rate at cMFBs, we used the described model of the active zone and included a release sensor at 20-nm distance from the nearest Ca^{2+} channel. The release scheme was taken from ref. 75 and was adjusted for physiological temperature and a release probability of 0.3 (76). To test the sensitivity of our findings on the used release scheme, we systematically compared several release schemes as explained in detail in Fig. S6.

Data Analysis. Statistical comparisons were performed via two-sided paired or unpaired Student *t* tests; $P < 0.05$ was considered significant. Means are expressed ± SEM except where stated.

ACKNOWLEDGMENTS. We thank David A. DiGregorio, Jens Eilers, Hartmut Schmidt, Beat Schwaller, and R. Angus Silver for critically reading the manuscript. This work was supported by Heisenberg Program of the German Research Foundation Grant HA 6386/2-2 and 3-2 (to S.H.) and National Science Foundation Grant DMS-0817703 (to V.M.).

1. Neher E, Sakaba T (2008) Multiple roles of calcium ions in the regulation of neurotransmitter release. *Neuron* 59(6):861–872.
2. Llinás R, Sugimori M, Silver RB (1992) Microdomains of high calcium concentration in a presynaptic terminal. *Science* 256(5057):677–679.
3. Schwaller B (2010) Cytosolic Ca^{2+} buffers. *Cold Spring Harb Perspect Biol* 2(11):a004051.
4. Neher E, Augustine GJ (1992) Calcium gradients and buffers in bovine chromaffin cells. *J Physiol* 450:273–301.
5. Eggermann E, Bucurenciu I, Goswami SP, Jonas P (2012) Nanodomain coupling between Ca^{2+} channels and sensors of exocytosis at fast mammalian synapses. *Nat Rev Neurosci* 13(1):7–21.
6. Rancz EA, et al. (2007) High-fidelity transmission of sensory information by single cerebellar mossy fibre boutons. *Nature* 450(7173):1245–1248.
7. Saviane C, Silver RA (2006) Fast vesicle reloading and a large pool sustain high bandwidth transmission at a central synapse. *Nature* 439(7079):983–987.
8. Ritzau-Jost A, et al. (2014) Ultrafast action potentials mediate kilohertz signaling at a central synapse. *Neuron* 84(1):152–163.
9. Müller M, Felmy F, Schwaller B, Schneggenburger R (2007) Parvalbumin is a mobile presynaptic Ca^{2+} buffer in the calyx of Held that accelerates the decay of Ca^{2+} and short-term facilitation. *J Neurosci* 27(9):2261–2271.
10. Burrone J, Neves G, Gomis A, Cooke A, Lagnado L (2002) Endogenous calcium buffers regulate fast exocytosis in the synaptic terminal of retinal bipolar cells. *Neuron* 33(1):101–112.
11. Thomsen LB, Jörntell H, Midtgaard J (2010) Presynaptic calcium signalling in cerebellar mossy fibres. *Front Neural Circuits* 4:1.

12. Beierlein M, Gee KR, Martin VV, Regehr WG (2004) Presynaptic calcium measurements at physiological temperatures using a new class of dextran-conjugated indicators. *J Neurophysiol* 92(1):591–599.
13. Yasuda R, et al. (2004) Imaging calcium concentration dynamics in small neuronal compartments. *Sci STKE* 2004(219):pl5.
14. Helmchen F, Borst JG, Sakmann B (1997) Calcium dynamics associated with a single action potential in a CNS presynaptic terminal. *Biophys J* 72(3):1458–1471.
15. Jackson MB, Redman SJ (2003) Calcium dynamics, buffering, and buffer saturation in the boutons of dentate granule-cell axons in the hilus. *J Neurosci* 23(5):1612–1621.
16. Scott R, Rusakov DA (2006) Main determinants of presynaptic Ca^{2+} dynamics at individual mossy fiber-CA3 pyramidal cell synapses. *J Neurosci* 26(26):7071–7081.
17. Neher E (1995) The use of fura-2 for estimating Ca buffers and Ca fluxes. *Neuropharmacology* 34(11):1423–1442.
18. Lee SH, Rosenmund C, Schwaller B, Neher E (2000) Differences in Ca^{2+} buffering properties between excitatory and inhibitory hippocampal neurons from the rat. *J Physiol* 525(Pt 2):405–418.
19. Maravall M, Mainen ZF, Sabatini BL, Svoboda K (2000) Estimating intracellular calcium concentrations and buffering without wavelength ratioing. *Biophys J* 78(5):2655–2667.
20. Nakamura Y, et al. (2015) Nanoscale Distribution of Presynaptic Ca^{2+} Channels and Its Impact on Vesicular Release during Development. *Neuron* 85(1):145–158.
21. Brenowitz SD, Regehr WG (2007) Reliability and heterogeneity of calcium signaling at single presynaptic boutons of cerebellar granule cells. *J Neurosci* 27(30):7888–7898.
22. Koester HJ, Sakmann B (2000) Calcium dynamics associated with action potentials in single nerve terminals of pyramidal cells in layer 2/3 of the young rat neocortex. *J Physiol* 529(Pt 3):625–646.
23. Lee SH, Schwaller B, Neher E (2000) Kinetics of Ca^{2+} binding to parvalbumin in bovine chromaffin cells: Implications for $[Ca^{2+}]$ transients of neuronal dendrites. *J Physiol* 525(Pt 2):419–432.
24. Sala F, Hernández-Cruz A (1990) Calcium diffusion modeling in a spherical neuron. Relevance of buffering properties. *Biophys J* 57(2):313–324.
25. Neher E, Taschenberger H (2013) Transients in global Ca^{2+} concentration induced by electrical activity in a giant nerve terminal. *J Physiol* 591(Pt 13):3189–3195.
26. Jörntell H, Ekerot CF (2006) Properties of somatosensory synaptic integration in cerebellar granule cells in vivo. *J Neurosci* 26(45):11786–11797.
27. Sargent PB, Saviane C, Nielsen TA, DiGregorio DA, Silver RA (2005) Rapid vesicular release, quantal variability, and spillover contribute to the precision and reliability of transmission at a glomerular synapse. *J Neurosci* 25(36):8173–8187.
28. Kim MH, Korogod N, Schneggenburger R, Ho WK, Lee SH (2005) Interplay between Na^{+}/Ca^{2+} exchangers and mitochondria in Ca^{2+} clearance at the calyx of Held. *J Neurosci* 25(26):6057–6065.
29. Collin T, et al. (2005) Developmental changes in parvalbumin regulate presynaptic Ca^{2+} signaling. *J Neurosci* 25(1):96–107.
30. Kaeser PS, Regehr WG (2014) Molecular mechanisms for synchronous, asynchronous, and spontaneous neurotransmitter release. *Annu Rev Physiol* 76:333–363.
31. Neher E (1998) Usefulness and limitations of linear approximations to the understanding of Ca++ signals. *Cell Calcium* 24(5-6):345–357.
32. Vanselow BK, Keller BU (2000) Calcium dynamics and buffering in oculomotor neurones from mouse that are particularly resistant during amyotrophic lateral sclerosis (ALS)-related motoneurone disease. *J Physiol* 525(Pt 2):433–445.
33. Habets RL, Borst JG (2006) An increase in calcium influx contributes to post-tetanic potentiation at the rat calyx of Held synapse. *J Neurophysiol* 96(6):2868–2876.
34. Xu T, Naraghi M, Kang H, Neher E (1997) Kinetic studies of Ca^{2+} binding and Ca^{2+} clearance in the cytosol of adrenal chromaffin cells. *Biophys J* 73(1):532–545.
35. Zhou Z, Neher E (1993) Mobile and immobile calcium buffers in bovine adrenal chromaffin cells. *J Physiol* 469:245–273.
36. Helmchen F, Imoto K, Sakmann B (1996) Ca^{2+} buffering and action potential-evoked Ca^{2+} signaling in dendrites of pyramidal neurons. *Biophys J* 70(2):1069–1081.
37. Matthews EA, Schoch S, Dietrich D (2013) Tuning local calcium availability: Cell-type-specific immobile calcium buffer capacity in hippocampal neurons. *J Neurosci* 33(36):14431–14445.
38. Maeda H, Ellis-Davies GC, Ito K, Miyashita Y, Kasai H (1999) Supralinear Ca^{2+} signaling by cooperative and mobile Ca^{2+} buffering in Purkinje neurons. *Neuron* 24(4):989–1002.
39. Sabatini BL, Oertner TG, Svoboda K (2002) The life cycle of Ca^{2+} ions in dendritic spines. *Neuron* 33(3):439–452.
40. Tank DW, Regehr WG, Delaney KR (1995) A quantitative analysis of presynaptic calcium dynamics that contribute to short-term enhancement. *J Neurosci* 15(12):7940–7952.
41. Babai N, Kochubey O, Keller D, Schneggenburger R (2014) An alien divalent ion reveals a major role for Ca^{2+} buffering in controlling slow transmitter release. *J Neurosci* 34(38):12622–12635.
42. Baimbridge KG, Celio MR, Rogers JH (1992) Calcium-binding proteins in the nervous system. *Trends Neurosci* 15(8):303–308.
43. Eggermann E, Jonas P (2012) How the 'slow' Ca^{2+} buffer parvalbumin affects transmitter release in nanodomain-coupling regimes. *Nat Neurosci* 15(1):20–22.
44. Faas GC, Schwaller B, Vergara JL, Mody I (2007) Resolving the fast kinetics of cooperative binding: Ca^{2+} buffering by calretinin. *PLoS Biol* 5(11):e311.
45. Schwaller B (2009) The continuing disappearance of "pure" Ca^{2+} buffers. *Cell Mol Life Sci* 66(2):275–300.
46. Gabso M, Neher E, Spira ME (1997) Low mobility of the Ca^{2+} buffers in axons of cultured Aplysia neurons. *Neuron* 18(3):473–481.
47. Vyleta NP, Jonas P (2014) Loose coupling between Ca^{2+} channels and release sensors at a plastic hippocampal synapse. *Science* 343(6171):665–670.
48. Edmonds B, Reyes R, Schwaller B, Roberts WM (2000) Calretinin modifies presynaptic calcium signaling in frog saccular hair cells. *Nat Neurosci* 3(8):786–790.
49. Pangršič T, et al. (2015) EF-hand protein Ca^{2+} buffers regulate Ca^{2+} influx and exocytosis in sensory hair cells. *Proc Natl Acad Sci USA* 112(9):E1028–E1037.
50. Soler-Llavina GJ, Sabatini BL (2006) Synapse-specific plasticity and compartmentalized signaling in cerebellar stellate cells. *Nat Neurosci* 9(6):798–806.
51. Matveev V, Zucker RS, Sherman A (2004) Facilitation through buffer saturation: Constraints on endogenous buffering properties. *Biophys J* 86(5):2691–2709.
52. Chamberland S, Evstratova A, Tóth K (2014) Interplay between synchronization of multivesicular release and recruitment of additional release sites support short-term facilitation at hippocampal mossy fiber to CA3 pyramidal cells synapses. *J Neurosci* 34(33):11032–11047.
53. Hámori J, Somogyi J (1983) Differentiation of cerebellar mossy fiber synapses in the rat: A quantitative electron microscope study. *J Comp Neurol* 220(4):365–377.
54. Xu-Friedman MA, Regehr WG (2003) Ultrastructural contributions to desensitization at cerebellar mossy fiber to granule cell synapses. *J Neurosci* 23(6):2182–2192.
55. DiGregorio DA, Peskoff A, Vergara JL (1999) Measurement of action potential-induced presynaptic calcium domains at a cultured neuromuscular junction. *J Neurosci* 19(18):7846–7859.
56. Serulle Y, Sugimori M, Llinás RR (2007) Imaging synaptosomal calcium concentration microdomains and vesicle fusion by using total internal reflection fluorescent microscopy. *Proc Natl Acad Sci USA* 104(5):1697–1702.
57. Becherer U, Moser T, Stühmer W, Oheim M (2003) Calcium regulates exocytosis at the level of single vesicles. *Nat Neurosci* 6(8):846–853.
58. Frank T, Khimich D, Neef A, Moser T (2009) Mechanisms contributing to synaptic Ca^{2+} signals and their heterogeneity in hair cells. *Proc Natl Acad Sci USA* 106(11):4483–4488.
59. Svoboda K (2004) Do spines and dendrites distribute dye evenly? *Trends Neurosci* 27(8):445–446.
60. Schneggenburger R (2005) Ca^{2+} Uncaging in Nerve Terminals. *Imaging in Neuroscience and Development*, eds Yuste R, Konnerth A (Cold Spring Harbor Laboratory Press, Cold Spring Harbor, NY), pp 415–419.
61. Woehler A, Lin KH, Neher E (2014) Calcium-buffering effects of gluconate and nucleotides, as determined by a novel fluorimetric titration method. *J Physiol* 592(Pt 22):4863–4875.
62. Aponte Y, Bischofberger J, Jonas P (2008) Efficient Ca^{2+} buffering in fast-spiking basket cells of rat hippocampus. *J Physiol* 586(8):2061–2075.
63. Koch C (1999) *Biophysics of Computation Information Processing in Single Neurons* (Oxford Univ Press, New York).
64. Pan B, Zucker RS (2009) A general model of synaptic transmission and short-term plasticity. *Neuron* 62(4):539–554.
65. Meinrenken CJ, Borst JGG, Sakmann B (2002) Calcium secretion coupling at calyx of Held governed by nonuniform channel-vesicle topography. *J Neurosci* 22(5):1648–1667.
66. Schmidt H, et al. (2013) Nanodomain coupling at an excitatory cortical synapse. *Curr Biol* 23(3):244–249.
67. Matveev V, Sherman A, Zucker RS (2002) New and corrected simulations of synaptic facilitation. *Biophys J* 83(3):1368–1373.
68. Smith PD, Liesegang GW, Berger RL, Czerlinski G, Podolsky RJ (1984) A stopped-flow investigation of calcium ion binding by ethylene glycol bis(beta-aminoethyl ether)-N, N′-tetraacetic acid. *Anal Biochem* 143(1):188–195.
69. Naraghi M, Neher E (1997) Linearized buffered Ca^{2+} diffusion in microdomains and its implications for calculation of $[Ca^{2+}]$ at the mouth of a calcium channel. *J Neurosci* 17(18):6961–6973.
70. Nägerl UV, Novo D, Mody I, Vergara JL (2000) Binding kinetics of calbindin-D(28k) determined by flash photolysis of caged Ca(2+). *Biophys J* 79(6):3009–3018.
71. Sheng J, et al. (2012) Calcium-channel number critically influences synaptic strength and plasticity at the active zone. *Nat Neurosci* 15(7):998–1006.
72. Ermolyuk YS, et al. (2012) Independent regulation of basal neurotransmitter release efficacy by variable $Ca^{2}+$ influx and bouton size at small central synapses. *PLoS Biol* 10(9):e1001396.
73. Holderith N, et al. (2012) Release probability of hippocampal glutamatergic terminals scales with the size of the active zone. *Nat Neurosci* 15(7):988–997.
74. Scimemi A, Diamond JS (2012) The number and organization of Ca^{2+} channels in the active zone shapes neurotransmitter release from Schaffer collateral synapses. *J Neurosci* 32(50):18157–18176.
75. Wang LY, Neher E, Taschenberger H (2008) Synaptic vesicles in mature calyx of Held synapses sense higher nanodomain calcium concentrations during action potential-evoked glutamate release. *J Neurosci* 28(53):14450–14458.
76. Hallermann S, et al. (2010) Bassoon speeds vesicle reloading at a central excitatory synapse. *Neuron* 68(4):710–723.